Journal of Alloys and Compounds xxx (xxxx) xxx

Contents lists available at ScienceDirect

Journal of Alloys and Compounds

journal homepage: http://www.elsevier.com/locate/jalcom

Using a Couette–Taylor vortex flow reactor to prepare a uniform and highly stable $Li[Ni_{0\cdot80}Co_{0\cdot15}Al_{0.05}]O_2$ cathode material

Manojkumar Seenivasan [a, c], Chun-Chen Yang [a, c, e, *], She-huang Wu [a, b], Wen-Chen Chien [a, c], Yi-Shiuan Wu [a], Rajan Jose [d], Shingjiang Jessie Lue [e, f, g]

[a] Battery Research Center of Green Energy, Ming Chi University of Technology, New Taipei City, 24301, Taiwan, ROC
[b] Graduate Institute of Science and Technology, National Taiwan University of Science and Technology, 43, Sec. 4, Keelung Rd., Taipei, 106, Taiwan, ROC
[c] Department of Chemical Engineering, Ming Chi University of Technology, New Taipei City, 24301, Taiwan, ROC
[d] Nanostructured Renewable Energy Materials Laboratory, Faculty of Industrial Sciences and Technology, University Malaysia Pahang, 26300, Kuantan, Malaysia
[e] Department of Chemical and Materials Engineering, and Green Technology Research Center, Chang Gung University, Taoyuan City, 333, Taiwan, ROC
[f] Department of Radiation Oncology, Chang Gung Memorial Hospital, Taoyuan City, 333, Taiwan, ROC
[g] Department of Safety, Health and Environmental Engineering, Ming Chi University of Technology, New Taipei City, 243, Taiwan, ROC

ARTICLE INFO

Article history:
Received 19 June 2020
Received in revised form
24 July 2020
Accepted 13 October 2020
Available online xxx

Keywords:
Li-ion batteries
$LiNi_{0\cdot80}Co_{0\cdot15}Al_{0\cdot05}O_2$
High rate capability
Co-precipitation
Couette–Taylor flow reactor
Calcination temperature

ABSTRACT

This study mainly focuses on the preparation technique of Ni-rich NCA hydroxide by a Couette–Taylor flow reactor (CTFR), by systematically optimizing the preparation parameters, including cylinder rotation speed and calcination temperature to study its electrochemical performance. Because of the uniform mixing and constant fluid motion of the Taylor vortex, we obtained spherical and uniform $Ni_{0\cdot80}Co_{0\cdot15}Al_{0\cdot05}(OH)_2$ particles. The rotation speed of the inner cylinder determined the degrees of particle agglomeration and growth. X-ray diffraction and Rietveld refinement revealed that the sample prepared at 600 rpm had relatively large particles and a high degree of crystallinity; when calcined to 750 °C, it featured much smaller primary particles, a comparatively lower degree of cation mixing, and better layer structure ordering. The Ni-rich $LiNi_{0\cdot80}Co_{0\cdot15}Al_{0\cdot05}O_2$ prepared under the optimal conditions delivered a high discharge capacity of 190.6 mAh g^{-1} at 0.1C, on par with that of commercially available NCA powders; it also exhibited a remarkable improvement in rate capability, with a discharge capacity of 138 mAh g^{-1} at 10C (101 mAh g^{-1} for a commercial sample). In long cycle life tests, the prepared NCA sample retained a high capacity (87.4%) after 100 cycles at 1C, compared with 70.0% for the commercial sample. Furthermore, cyclic voltammetry and electrochemical impedance spectroscopy demonstrated the importance of the calcination temperature on the electrochemical performance and structural stability of our Ni-rich cathodes. Our as-prepared NCA cathode materials, obtained using a CTFR, appear to have great potential for application in Li-ion batteries.

1. Introduction

The search for sustainable renewable energy sources to replace traditional energy sources (e.g., fossil fuels) has led to major developments in green energy and its storage [1–4]. Among the possible electrical energy storage devices, Li-ion batteries (LIBs) have, in particular, revolutionized access to portable electronic devices and electric vehicles (EV) in the last two decades because of their high gravimetric and volumetric energy densities [5–8]. Lithium transition metal oxides are some the most researched materials for use as positive electrodes in LIBs. Although $LiNiO_2$-type cathodes are very attractive for their high specific capacities and relatively high working voltages (>3.6 V vs. Li), delithiated $LiNiO_2$ that is induced at high temperatures is very unstable because it leads to the formation of Ni^{2+} rather than Ni^{3+}, resulting in irregular stoichiometries in the system. Moreover, the generated Ni^{2+} often migrates to the Li^+ layer, causing an irreversible loss of valuable capacity. To overcome these shortcomings, several transition metals have been tested as substitutes at Ni sites to improve the structural and electrochemical stability of Ni-rich oxide cathode

---

* Corresponding author. Battery Research Center of Green Energy, Ming Chi University of Technology, New Taipei City, 24301, Taiwan, ROC.
E-mail address: ccyang@mail.mcut.edu.tw (C.-C. Yang).

https://doi.org/10.1016/j.jallcom.2020.157594
0925-8388/© 2020 Elsevier B.V. All rights reserved.

Please cite this article as: M. Seenivasan, C.-C. Yang, S.-h. Wu *et al.*, Using a Couette–Taylor vortex flow reactor to prepare a uniform and highly stable $Li[Ni_{0\cdot80}Co_{0\cdot15}Al_{0.05}]O_2$ cathode material, Journal of Alloys and Compounds, https://doi.org/10.1016/j.jallcom.2020.157594

materials. The conventional $Li_{1-x}CoO_2$ becomes unstable when delithiated with voltages above 4.3 V ($x > 0.5$). So, replacing Co with Ni in the layered structure results in higher utilization of lithium, resulting a capacity of 220 mAh g^{-1}. The most common substituted forms of Ni-rich oxides are $LiNi_{0.8}Co_{0.1}Mn_{0.1}O_2$ and $LiNi_{0.80}Co_{0.15}Al_{0.05}O_2$, where Co, Mn and Al were introduced to stabilize the thermal instability of the Ni-rich layered oxides near the fully charged (delithiated) state or at high temperature preventing from structural collapse [9–12].

Layered $LiNi_{0.8}Co_{0.15}Al_{0.05}O_2$ is a particularly promising cathode material because of its high energy density, low cost, stability, and cyclability [13]. It does, however, have a few drawbacks—poor thermal stability, structural instability, and the need for innovative techniques when formed using conventional preparation methods—that have inhibited its commercialization. Until now, various conventional synthetic methods were used to prepare Ni-rich cathode materials, including sol–gel synthesis [14], solid state methods [15], spray-drying [16], and co-precipitation method [17], the latter is most widely used to obtain particles of ternary transition metal hydroxides having homogenous distributions and spherical shapes.

Because crystal agglomeration is a factor that determines structural stability during intense Li^+ de/intercalation of cathodes and; thereby, determines their electrochemical properties. a Couette–Taylor flow vortex is highly efficient medium for the preparation of Ni-rich hydroxides in a homogenous phase and with spherically intact secondary particles. By controlling the reaction parameters, e.g., reaction temperature, pH, mean residence time, and rotation speed, precipitated particles having a desired shape and size can be prepared effectively, even on large scales [18]. Taylor flow has been used previously in, for example, the crystallization of calcium carbonate [19], barium sulfate [20], and graphene oxide [21]; the polymerization of styrene [22], and vinyl acetate [23]; and the cooling crystallization of sulfamerzine [24] and L-lysine [25].

Much effort has been exerted to improve the thermal stability and electrochemical performance of Ni-rich cathode materials. Some approaches have included adjusting the metal composition [26–28], surface modification [29,30], structural re-design [11,12,31], changing the surface phase [32], improving the preparation techniques [33,34], post-calcination treatments [35], and varying the calcination atmosphere [36] with various effects on the performance and properties of the resulting as-prepared Ni-rich cathodes. The calcination temperature is a particularly crucial parameter determining the particle size and electrochemical activity of a material. By optimizing the calcination conditions, we suspected that it might be possible to prepare highly applicable Ni-rich cathodes such as nickel–cobalt–aluminum (NCA) and nickel–cobalt–manganese (NCM).

In this study, we developed a method for the preparation of NCA hydroxides in a novel Couette–Taylor flow reactor (CTFR) and examined the effect of the preparation conditions, including the rotation speed, on the cathode materials. Furthermore, we evaluated the electrochemical properties of cathodes calcined at various temperatures in terms of their crystal structures, conductivities, stabilities, high rate performances, and cyclabilities.

2. Experimental methods

2.1. Material synthesis

$[Ni_{0.80}Co_{0.15}Al_{0.05}](OH)_2$ was prepared through a continuous co-precipitation method in a CTFR having a working volume of 1 L (Fig. 1). An aqueous solution of transition metal sulfates of nickel sulfate ($NiSO_4 \cdot 6H_2O$), cobalt sulfate ($CoSO_4 \cdot 7H_2O$), and aluminum sulfate [$Al_2(SO_4)_3 \cdot 16H_2O$] at an appropriate stoichiometry was prepared by adding the salts to de-ionized water and stirring until they had dissolved; the total concentration of Ni, Co, and Al in the reactant solution was fixed at 2 mol L^{-1}. Sodium hydroxide (NaOH) was used as the hydroxyl reactant and ammonium hydroxide (NH_4OH) as the chelating agent for the co-precipitation reaction **(Fig. S1)**. The concentration ratio of the prepared metal solution to NaOH was set at 1:2; that of the metal solution to NH_4OH was set at 1:3. All chemicals were of analytical grade (Alfa Aesar, Aldrich, or J. T. Baker) and were used directly without purification.

The CTFR reaction chamber was initially filled with de-ionized water; all the reactant solutions were pumped slowly into the chamber separately at a defined flow rate. The ratio of the flow rates of the metal solution to NH_4OH was set at 3:1. The pH of the reactant solutions in the reaction chamber was controlled precisely to 11.0 by adjusting the flow rate of the NaOH solution throughout the reaction process. For the formation of spherical NCA hydroxide particles, the precipitation reactions in the CTFR were performed at a reaction temperature of 60 °C, a pH of 11.0, and an inner cylinder rotation speed of 600, 900, or 1200 rpm. Finally, the co-precipitated NCA hydroxides were collected from the reactor, quickly washed several times with de-ionized water and ethanol, filtered, and dried at 120 °C for 12 h. To synthesize $Li[Ni_{0.80}Co_{0.15}Al_{0.05}]O_2$, the prepared $[Ni_{0.8}Co_{0.15}Al_{0.05}](OH)_2$ powder was mixed homogenously with $LiOH \cdot H_2O$ at a molar ratio of 1:1.05. The mixture was precalcined at 550 °C for 6 h, calcined at 750, 775, or 800 °C for 15 h under a steady flow of O_2 (heating rate: 2 °C min^{-1}), and cooled in controlled steps. The resulting samples are named herein as NCA-750, NCA-775, and NCA-800, respectively.

2.2. Characterization and electrochemical measurements

The crystal structure of the synthesized cathode material was analyzed using powder X-ray diffraction (XRD; Bruker D2 diffractometer, Germany; operated at 40 kV and 50 mA) and CuK-α radiation in the 2θ range 10–70°. The particle sizes, morphologies, and microstructures were examined using dynamic light scattering (DLS; Beckman Coulter LS 133 2, USA), scanning electron microscopy (SEM; Hitachi, Japan), and high-resolution transmission electron microscopy (HR-TEM; JEOL JEM–2100F, Japan). The valence states of Ni, Co, and Al ions were examined by X-ray photoelectron spectroscopy (XPS) (PHI5600, PerkinElmer) and the XPS data was analyzed by XPSPEAK 4.1 software. The chemical compositions of the prepared hydroxide and oxide samples were determined using inductively coupled plasma optical emission spectroscopy (ICP-OES; Thermal, USA). Cyclic voltammetry (CV) and electrochemical impedance spectroscopy (EIS) were performed using an electrochemical workstation (AutoLab, Netherland) to study the electrochemical performance and interfacial impedance. The working electrode was the as-prepared cathode material; the counter electrode and the reference electrode were Li metal; the scan rate was 0.01 mV s^{-1}; and the scanning voltage range was 2.5–4.4 V. EIS was performed in the frequency range from 100 kHz to 0.01 Hz with an amplitude of 5 mV.

The electrochemical performance of the obtained cathode materials was evaluated using CR2032 coin-type half-cells. The positive electrodes were prepared by mixing a slurry of the active material, conductive carbon, and poly(vinylidene difluoride) (PVDF) at a weight ratio of 8:1:1 in *N*-methyl-2-pyrrolidone (NMP). The mixture was coated on an aluminum foil (20 μm, Aldrich) current collector, then dried in a vacuum oven at 60 and 120 °C to remove any moisture from the electrode surface. The electrodes were cut into circles having a diameter of 13 mm; the loading of the

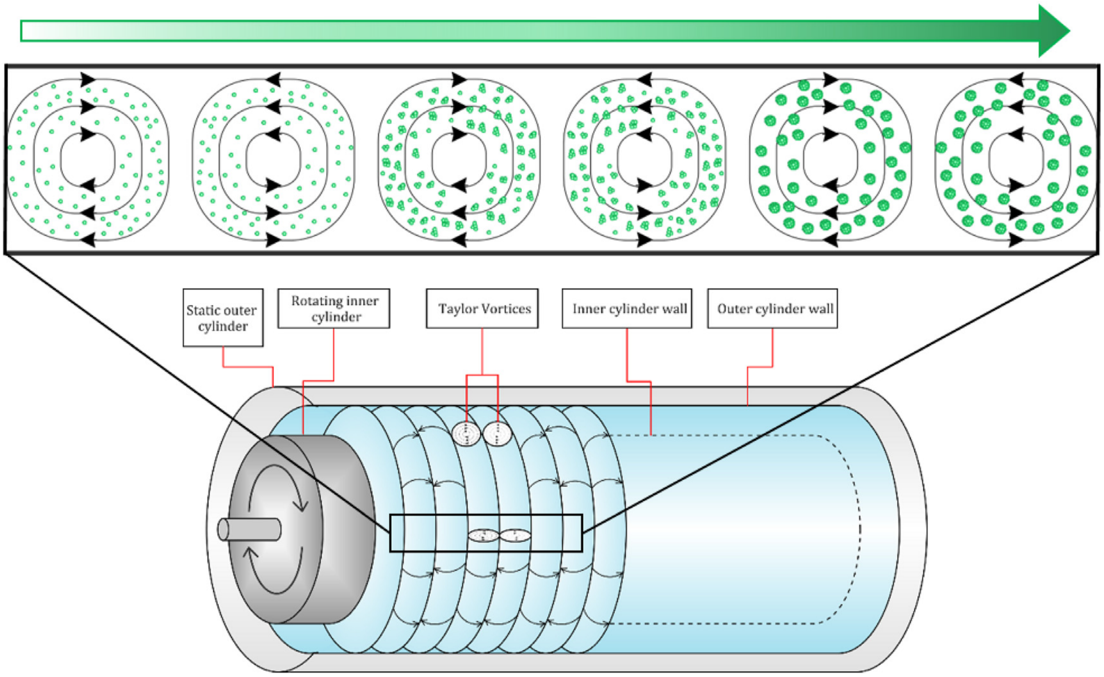

Fig. 1. Schematic representation of the working model of Taylor vortex flow in a CTFR.

active material was approximately 4 mg cm^{-2}. The electrodes were assembled into CR2032 coin-type half-cells in an Ar-filled glove box, using Li metal as the anode and a microporous polyethylene (PE) membrane (Celgard 2400, USA) as the separator. The electrolyte was a solution of 1 M $LiPF_6$ in ethylene carbonate (EC)/diethyl carbonate (DEC) (1:1, v/v). Galvanostatic charge/discharge cycle experiments were performed between 2.8 and 4.3 V (vs Li^+/Li) using a BT2043 charger (Arbin, USA), at 0.1 A at 25 °C. A current density of 1C was defined as 200 mA g^{-1}.

3. Results and discussion

3.1. Particle formation mechanism in Couette-Taylor flow

The CTFR was initially filled with pure water and then the metal sulfates were injected along with NaOH and the chelating agent NH_4OH to initiate the reaction in the chamber, as stated in eqns (1) and (2). Fig. 1 provides a schematic representation of the working model of the CTFR. Couette–Taylor flow is created between a static outer cylinder and a rotating inner cylinder. This Taylor vortex is made of couplets of inwardly rotating circular motion in the liquid. The onset of particle crystallization occurs in the beginning parts of the vortices and slowly moves through the chamber length, with gradual growth during the mean residence time, as shown in Fig. 1.

$$M^{2+} + nNH_3 \leftrightarrow NH_3)(NH_3)(NH_3)_n]^{2+} \tag{1}$$

$$NH_3)(NH_3)(NH_3)_n]^{2+} + 2OH^- \leftrightarrow M(OH)_2\downarrow + nNH_3 \tag{2}$$

where M = Ni, Co, Al.

The particle size of the hydroxide precursor can be controlled by many parameters, including the concentration of the reactants, the mean residence time, and the rotation speed. We measured the particle size of NCA hydroxides in the product suspension at regular intervals (Fig. 2a). The particles were quite large at the onset of the co-precipitation reaction but dropped to half of their size after about two times the mean residence time (i.e., after 8 h). The curve in Fig. 2a begins to plateau at about four times the mean residence time (i.e., after 16 h), indicative of steady state flow in the reaction chamber of the CTFR [18]. The NCA hydroxide particles obtained at different reaction times were shown in Fig. S2, as the particles looked clustered without proper shape up to 12h then after 16h the particles gained much better shape. After 20h the particles became uniformly shaped and distributed. This was confirmed by testing the size of the particles for samples obtained at regular time intervals shown in Fig. S3. The rotation speed also impacted the steady state flow. When the rotation speed was relatively high, the particles tended to be smaller initially and even smaller after the steady state of flow had been achieved. This trend occurred irrespective of the speed, only resulting in different particle sizes, implying that the speed was indeed a crucial parameter for controlling the particle size of the NCA hydroxide in the CTFR. Fig. 2b presents the particle shape and size distribution at steady state flow. A low rotation speed produced relatively large particles having irregular shapes; in contrast, a high rotation speed decreased the particle size and gave round particles. This contrast in particle shape and distribution according to the rotation speed originated from agglomeration of the crystals being controlled by the Taylor vortex fluid motion of the suspension.

The agglomeration of crystals in a Taylor vortex flow involves sequential nucleation and crystal growth, with the rotation speed having a direct impact. Initially, multiple crystal nuclei would form and collide, accumulating to form a cluster of particles in the Taylor vortex fluid motion, and eventually binding firmly through molecular growth to become solid agglomerates. The fluid shear force in the vortex can, however, break down these crystal clusters and prevent them from growing further. Therefore, at relatively low rotation speeds, the agglomerate particles were large and irregularly shaped. In contrast, when the fluid shear force was greater than the strength of physical bonding between the crystals, the aggregate particles were trimmed by the turbulent shear; therefore, they became rounder at relatively higher rotation speeds. The CTFR appears to have several advantages over a conventional

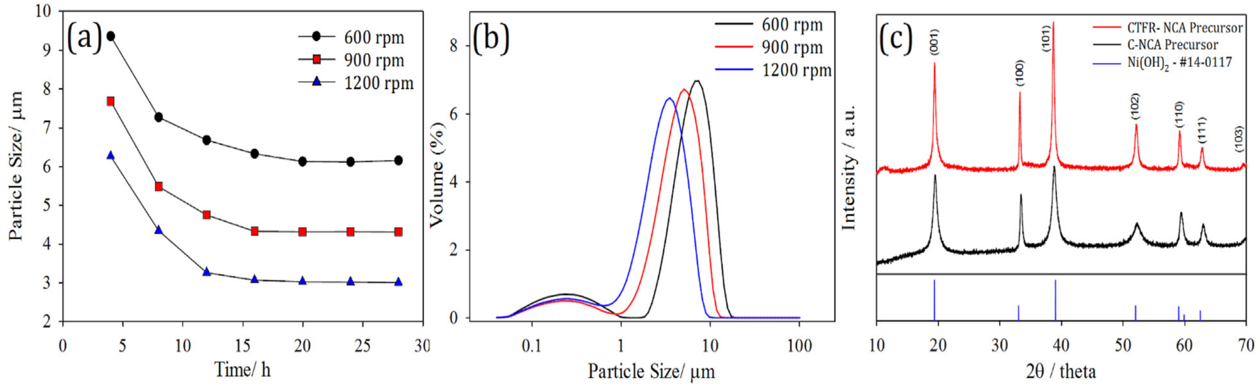

Fig. 2. (a) Typical steady state flow behavior of NCA hydroxides prepared in the CTFR. (b) Size distribution plots of NCA hydroxides prepared in the CTFR at various speeds obtained under steady-state flow. (c) Powder XRD patterns of the as-prepared $Ni_{0.80}Co_{0.15}Al_{0.05}(OH)_2$ and a commercially available NCA material.

continuous stirred-tank reactor (CSTR) or a mixed suspension mixed product removal (MSMPR) reactor when used for co-precipitation synthesis of Ni-rich hydroxides. For instance, a lower mean residence time required for the continuous crystallization process to attain optimum productivity (30–60 min for the CTFR; 270–720 min for the CSTR and MSMPR reactors) [37]. Because of the high fluid shear force in the CTFR, a low mean residence time is sufficient to produce particles having sizes of less than 5 µm; the random well-mixed motion in the CSTR and MSMPR reactors requires much longer mean residence times. Furthermore, large-scale production is highly efficient when using the Couette–Taylor reactor method with unlimited continuous feeding of the reactants, whereas it is limited by the reactor size in the CSTR because of batch processing.

3.2. Structure and morphologies

Fig. 3 displays SEM images of the NCA hydroxide samples prepared in the at various speeds. As stated earlier, the particles prepared at 600 rpm were large and elliptical (Fig. 3a), while those prepared at 900 and 1200 rpm (Fig. 3c and d) were smaller and spherical. The magnified image in Fig. 3b reveals that the primary particles were typically tiny flakes bound together to form secondary particles. This unique structure for the NCA hydroxide particles is similar to the crystal structure of β-$Ni(OH)_2$, confirming that the Co and Al atoms in the NCA particles were incorporated into the crystal structure as solid solutions [38]. Shown in Fig. 4 is the EDX mappings and line scan of precursor NCA hydroxide particles prepared by CTFR. The elemental mapping reveals the three metals Ni, Co, and Al were present uniformly in the particle. It further reveals the elemental composition of each metal present in the bulk phase. The results show that Ni, Co, and Al were at 78.5, 16.1 and 5.4%, respectively which confirms successful achievement of the targeted stoichiometric ratio.

Fig. 2c presents the XRD pattern of the $Ni_{0.80}Co_{0.15}Al_{0.05}(OH)_2$ sample prepared using the Couette–Taylor flow method and that of a commercial NCA precursor (Zhejiang Huayou Cobalt, China). All of the diffraction peaks could be indexed to the hexagonal phase of β-$Ni(OH)_2$ (JCPDS, #14–0117). No peaks for any impurity phase were evident, confirming that the product was of a pure phase [37,39]. The peaks in the pattern of the prepared NCA hydroxide were narrower and sharper than those of the C-NCA sample, indicating that the former had a highly crystalline structure. We recorded XRD patterns (Fig. 5) of the calcined samples NCA-750, NCA-775, and NCA-800 and performed Rietveld refinement analyses using TOPAS software (Table 1). All the diffraction peaks of these samples matched those of the standard $LiNiO_2$ pattern; therefore, they could be indexed to a layered α-$NaFeO_2$–type structure of R-3m space group, with no obvious impurities [40]. Fig. 5a reveals that, for all our samples, the peaks pairs (006/102) and (108/110) at 40 and 65° were split well, suggesting that the prepared samples had highly ordered crystalline layered structures [34,41–43]. ICP-OES analysis confirmed the chemical compositions of our as-prepared NCA hydroxides and oxides (Table 2). The hydroxides synthesized in the CTFR reactor and the oxides calcined at 750 °C possessed almost exactly their expected nominal designed stoichiometries.

As listed in Table 1, the lattice parameters *a* and *c* increased upon increasing the calcination temperature; the cell volume also increased accordingly. The *R*-factors R_{wp} and R_p are two important parameters when evaluating XRD refinement data; the values obtained are reliable and acceptable only when the *R*-factor is less than 10%. It is regarded that complete oxidation of Ni^{2+} to Ni^{3+} is quite difficult to achieve, even under a pure O_2 atmosphere, some Ni^{2+} ions would occupy the 3a sites of Li^+ ions, due to their similar ionic radii (Ni^{2+}: 0.069 nm; Li^+: 0.076 nm); this is a well-known phenomenon called cation mixing [35]. The degree of cation mixing in the crystal structure of an NCA material is usually characterized by the intensity ratio (R) of the peaks I_{003} and I_{104} [35]. Values of R higher than 1.2 represent a low degree of cation mixing, a small irreversible capacity loss, and therefore, good electrochemical performance [35,44]. The intensity ratios of our samples NCA-750, NCA-775, and NCA-800 were 1.810, 1.783, and 1.639, respectively—much greater than the recommended value and some of the values reported previously [28,33,35].

These results are consistent with the calculated degrees of cation mixing for all of our samples (Table 1), with NCA-750 having a lowest degree of cation mixing (1.9%) among them. The calcination temperature played an important role affecting the ordering of the layered structure in the primary particle. As the temperature increased, the crystallinity of the oxide particles increased, as did the degree of cation mixing. We attribute this behavior to an increase in the number of oxygen vacancies at high temperature, bringing more Ni^{2+} ions into the crystal structure and increasing the possibility of cation mixing, even though the crystallinity was good [28]. Therefore, we expected that the sample calcined at 750 °C would display favorable electrochemical performance, due to its moderate crystallinity and low degree of cation disorder.

Fig. 6 displays SEM and TEM images of our prepared $LiNi_{0.8}Co_{0.15}Al_{0.05}O_2$ samples, all of which comprised primary particles tightly packed into spherical particles having average sizes of approximately 5–6 µm. We expected these spherical morphologies would improve the energy densities and tap densities of the

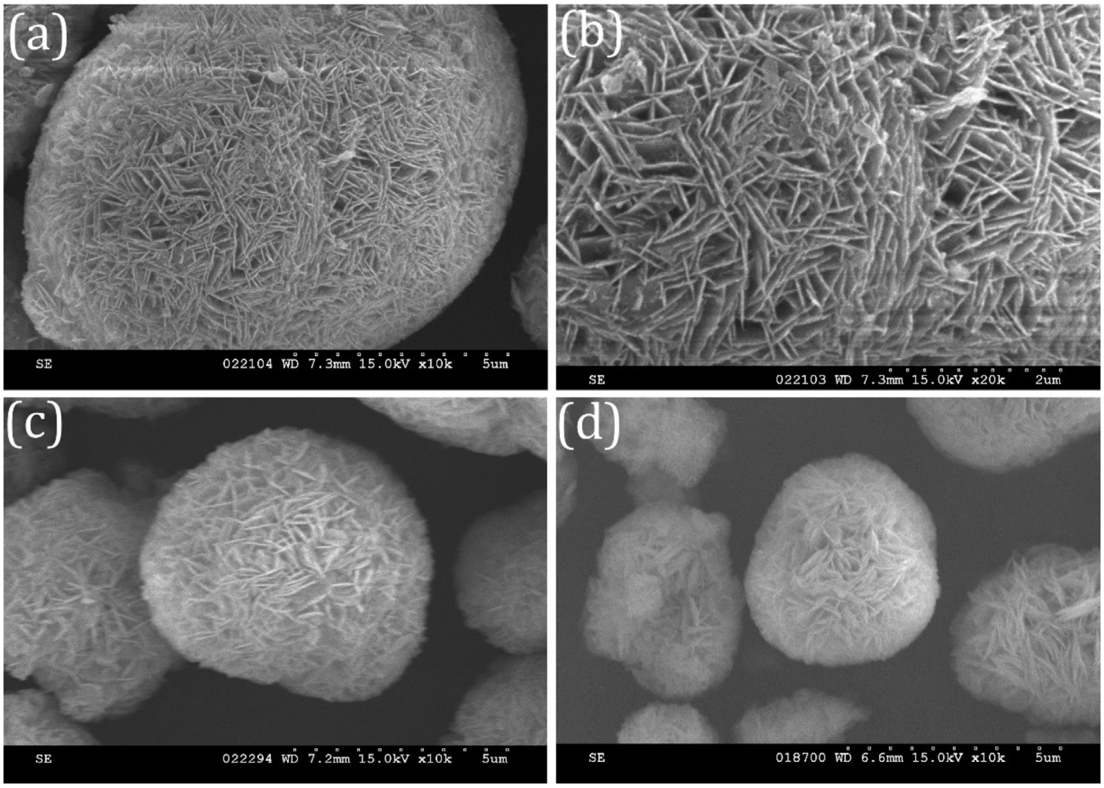

Fig. 3. (a) SEM images of NCA hydroxides prepared at (a, b) 600, (c) 900, and (d) 1200 rpm.

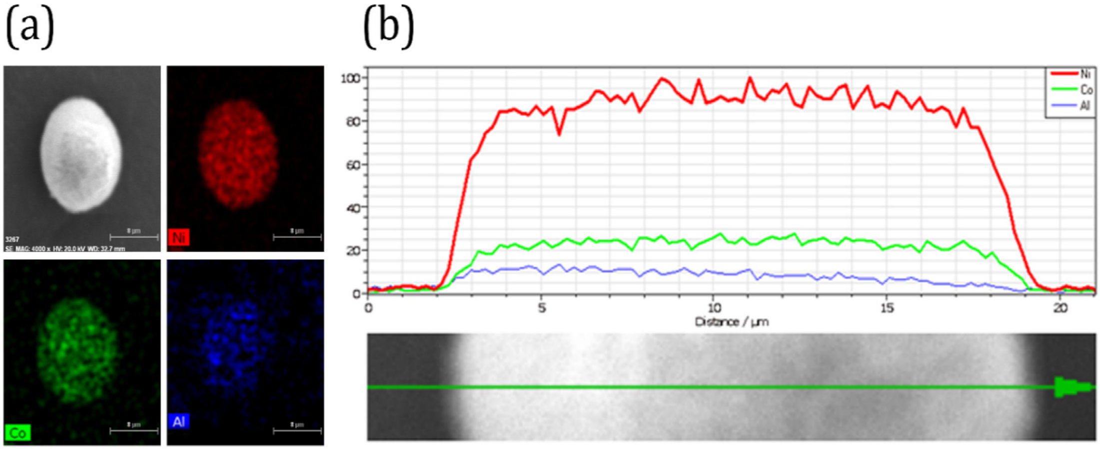

Fig. 4. (a) EDX mappings of Ni, Co and Al; (b) EDX line scans from the NCA hydroxide precursor prepared by CTFR.

cathode materials, due to the high volumes of the materials. Moreover, the sizes of the primary particles substantially increased upon increasing the calcination temperature, leading to better crystallinity and higher peak intensities. Fig. 6a–c reveal that the primary particles of NCA-750 and NCA-775 were polyhedral with sizes varying from 200 to 500 nm, growing significantly for NCA-800 into the range from 500 nm to 1 μm. The size of the primary particle plays a role in Li^+ diffusion during intercalation and deintercalation by affecting the Li^+ diffusion pathways [13,28]. For NCA-750, the primary particles were relatively small (compared with those of NCA-800), a potentially beneficial feature providing shorter diffusion pathways for Li^+ migration during charging and discharging.

To further analyze the surface components of the $LiNi_{0.8}Co_{0.15}Al_{0.05}O_2$ sample prepared at 750 °C for 15h, as shown in Fig. S4. Fig. S4a shows the XPS data for Ni 2p. After fitting the results, the binding energies of ~855.51 and ~857.18 eV correspond to $Ni2p_{3/2}$ of Ni^{2+} and Ni^{3+}, respectively. XPS data for Co 2p is shown in Fig. S4b. The peak at 779.21 eV is assigned to Co $2p_{3/2}$ whereas the peak at ~794.54 eV is assigned to the Co $2p_{1/2}$. The Al 2p XPS spectra is shown in Fig. S4c. The peak at 72.39 eV is assigned to Al $2p_{3/2}$ with Al in Al^{3+} state [45].

Fig. 6d provides a TEM image of NCA-750, revealing a clear interplanar spacing lattice of 0.469 nm, consistent with the (003) crystal planes of $LiNi_{0.8}Co_{0.15}Al_{0.05}O_2$. The well-ordered layered structure was present from the bulk phase to the surface areas,

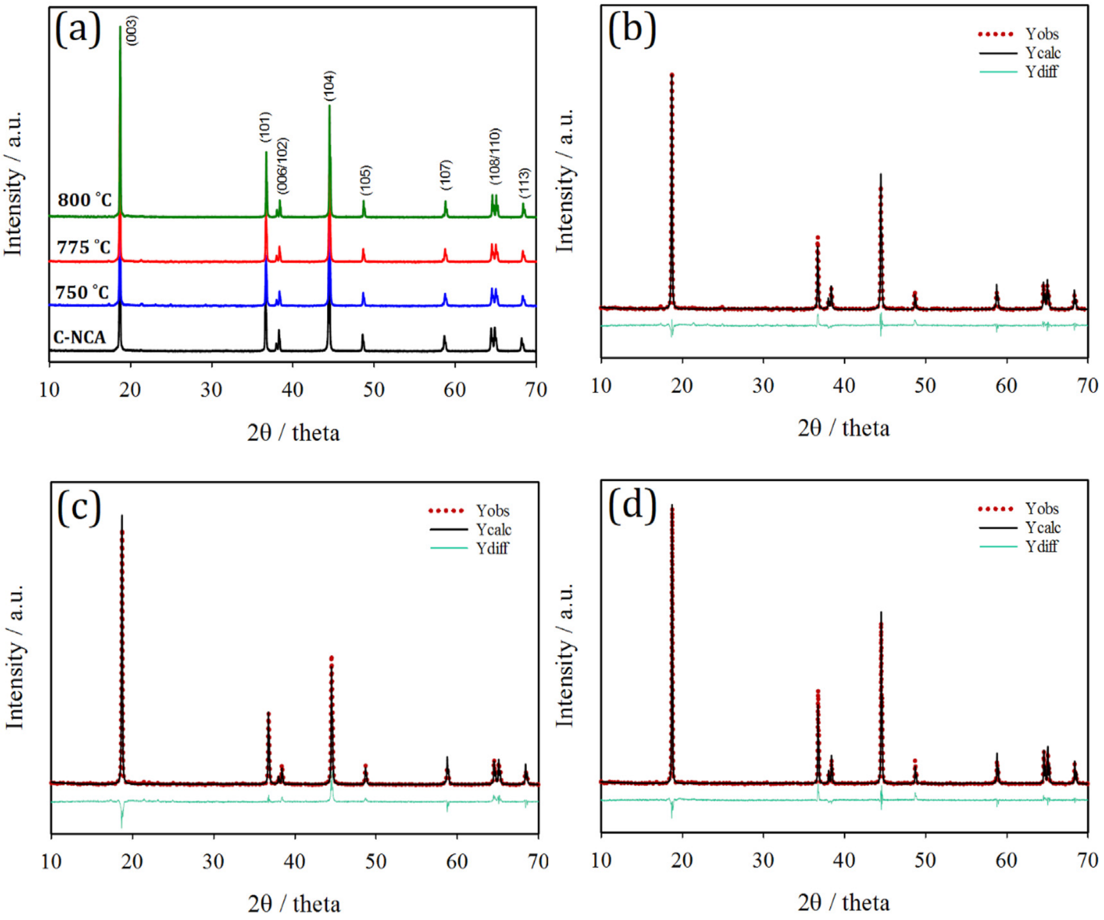

Fig. 5. (a) Powder XRD patterns of the prepared $LiNi_{0·8}Co_{0·15}Al_{0·05}O_2$ calcined at various temperatures. (b–d) Rietveld refinement patterns of the XRD data for the $LiNi_{0·8}Co_{0·15}Al_{0·05}O_2$ samples prepared at (b) 750, (c) 775, and (d) 800 °C.

Table 1
Obtained results of XRD Rietveld refinement analysis for $LiNi_{0·8}Co_{0·15}Al_{0·05}O_2$ materials synthesized at different calcining temperature.

Sample	a (Å)	c (Å)	c/a	V (Å^3)	R ($I_{(003)}/I_{(104)}$)	Ni occupancy	R_p/R_{wp} (%)
NCA-750	2.86342	14.16903	4.94828	100.61	1.8105	0.019	2.67/4.02
NCA-775	2.86402	14.17354	4.94882	100.68	1.7835	0.037	2.84/4.22
NCA-800	2.86465	14.17397	4.94788	100.72	1.6393	0.051	2.88/4.29

Table 2
Chemical compositions of samples obtained from ICP-OES analysis.

Prepared sample	Li (mol %)	Ni (mol %)	Co (mol %)	Al (mol %)
NCA hydroxide	–	0.799	0.161	0.0402
NCA	1.06	0.795	0.165	0.0430

suggesting a low amount of Li residue on the surface of this NCA cathode material. Fig. 6f presents the fast Fourier transform (FFT) pattern of the (003) plane as white dots, providing further evidence for a *d*-spacing of 4.69 Å. Fig. S5 shows the SEM image and EDX analysis of NCA-750 particle. The EDX elemental mapping images reveals that Ni, Co, and Al were uniformly distributed in the particles, as shown in Fig. S5b–d. The molar ratio of Ni, Co and Al identified from the EDX analysis showed 79.2, 15.4 and 5.4%, respectively, which is very consistent with the XRD Rietveld and ICP-OES analysis results.

3.3. Electrochemical performances

Electrochemical measurements were carried out to study the battery performances of our as-prepared cathode materials. Fig. 7a displays the initial charge/discharge profiles of all of the NCA samples in the potential range 2.8–4.3 V at a rate of 0.1C. As expected, each of our prepared samples exhibited a voltage profile typical of $LiNi_{0·80}Co_{0·15}Al_{0·05}O_2$. NCA-750 provided the highest capacity (190.6 mAh g^{-1}) with highest initial coulombic efficiency (91.1%) when compared with those of the other NCA materials. The NCA-775, NCA-800, and C-NCA samples exhibited initial discharge capacities of 187.3, 183.3, and 191.4 mAh g^{-1}, respectively, and coulombic efficiencies of 90.7, 88.7, and 88.5%, respectively. The lower coulombic efficiencies for the samples calcined at higher temperatures were presumably due to the increased number of Li^+ ion pathways in the much larger primary particles. We conclude that the temperature of heat treatment could, indeed, affect the discharge capacity of the cathode directly.

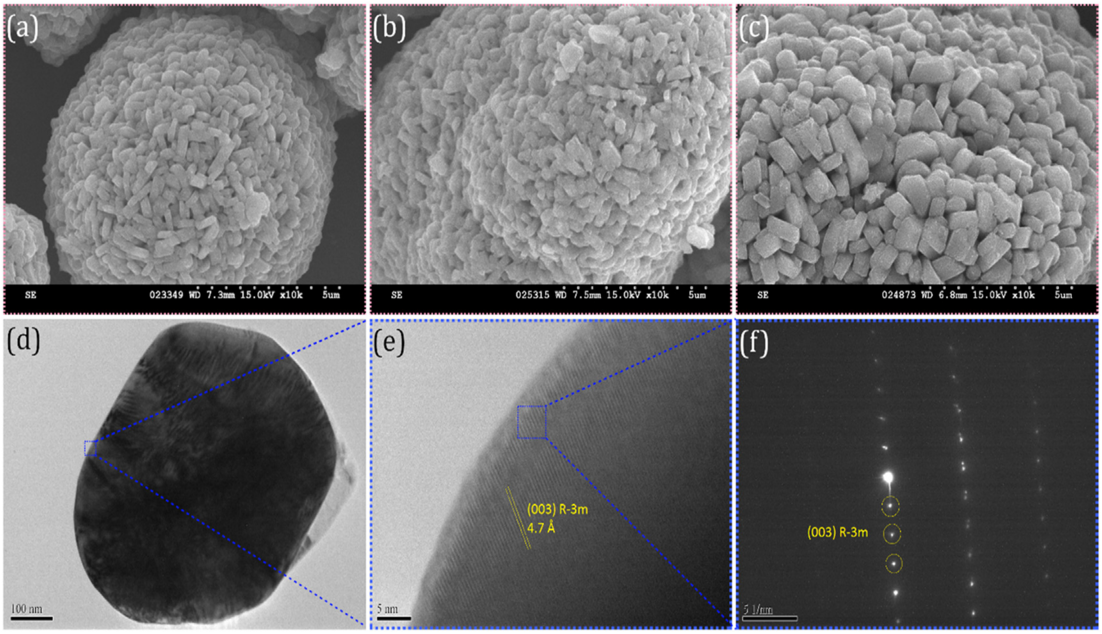

Fig. 6. (a–c) SEM images of the NCA samples prepared at (a) 750, (b) 775, and (c) 800 °C. (d, e) TEM and (f) FFT images of the NCA sample prepared at 750 °C.

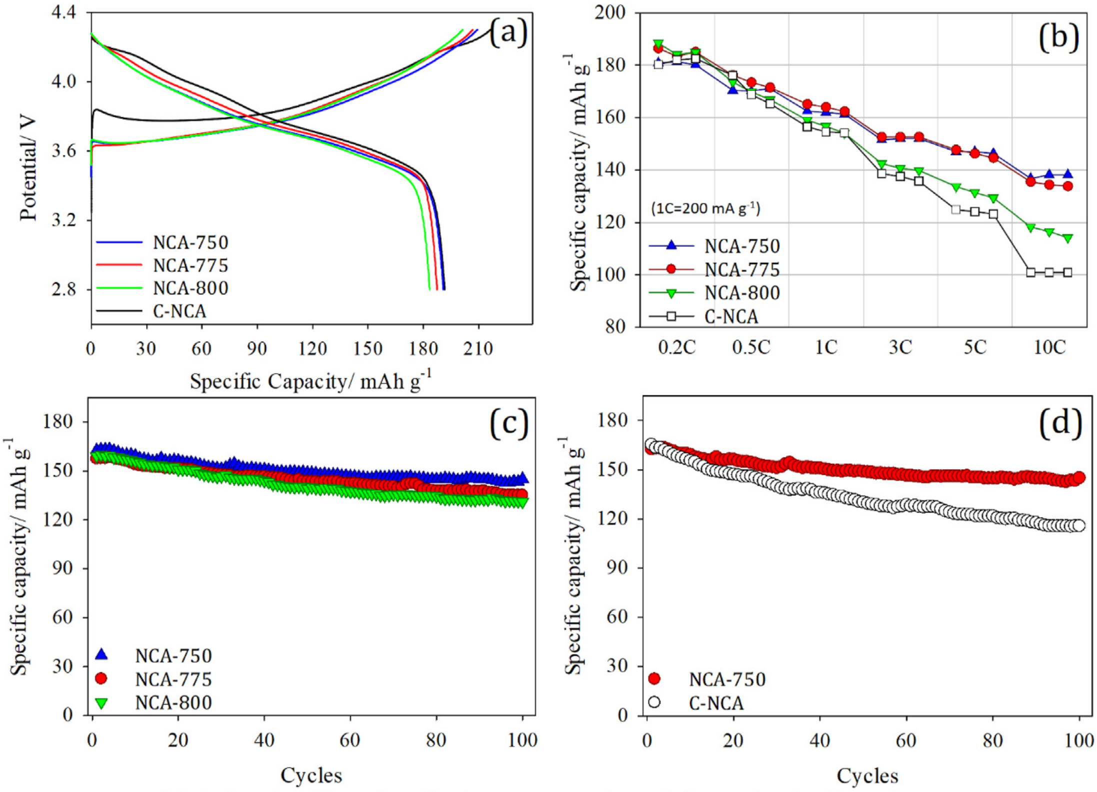

treatment could, indeed, affect the discharge capacity of the cathode directly.

Fig. 7. (a) Charge/discharge profiles of the prepared NCA samples and a commercial NCA sample. (b) Rate capabilities of all of the samples, measured at rates from 0.2C to 10C. (c) Cycling performance of the prepared samples at 1C. (d) Cycling performance of NCA-750 and the commercial sample. All tests were performed at potentials within 2.8–4.3 V and at 25 °C (1C = 200 mA g^{-1}).

High power density is another important characteristic affecting the practical EV applications of LIBs. We tested the rate capabilities of all of our cathodes in the discharge range of 0.2–10C at 25 °C with fixed charge rate at 0.2C (Fig. 7b). Although the specific discharge capacities at 0.2C of all of the NCA samples were similar, increasing the C-rate to 10C caused the NCA-750 cathode to exhibit a reversible capacity (138.1 mAh g^{-1}) higher than those of the NCA-775 and NCA-800 samples (134.4 and 116.6 mAh g^{-1}, respectively), with each of them higher than that (101 mAh g^{-1}) of the C-NCA cathode. A loss of capacity at higher C-rates is normally due to serious interfacial side reactions between the active material and the electrolyte, resulting in metal dissolution, structural collapse, and the formation of a thick solid electrolyte interphase (SEI) layer [46].

To investigate the structural stability of our prepared electrodes, we performed a cycle life study over 100 cycles at 1C/1C and 25 °C (Fig. 7c). The NCA-750 sample had an initial capacity of 162.7 mAh g^{-1} that faded to 145.1 mAh g^{-1} after the 100th cycle; this fairly high capacity retention (87.4%) was better than those of the NCA-775 and NCA-800 samples (85.8 and 82.4%, respectively). Furthermore, the electrochemical performance of the NCA-750 sample was greater than that of the commercial NCA sample, which had a capacity retention of only 70.0% (Fig. 7d). We attribute the improved capacity retention of NCA-750 to its superior kinetic reversibility and structural stability during Li^+ intercalation/deintercalation, due to its densely packed secondary particles and lower surface area. Table 3 compares the performance of some previously reported cathodes materials with that of our sample prepared using the CSTR. Figs. S6a and S6b display the 0.2–10C rate performances of the NCA-750 and C-NCA samples; Figs. S6c and S6d present their voltage profiles after 100 cycles at 1C. As the calcination temperature increased, the capacity retention decreased, presumably because of the bigger particles and the possibility of a large amount of SEI layer on the surface and longer diffusion paths for Li^+ ions. The prepared NCA-750 sample had an energy density of 618 Wh kg^{-1} during the initial cycle at 1C, almost similar to that (610 Wh kg^{-1}) of the C-NCA. Nevertheless, NCA-750 retained an energy density of 551 Wh kg^{-1} after the 100th cycle, whereas those of NCA-775 and NCA-800 were 514 and 498 Wh kg^{-1}, respectively, while that of C-NCA was even lower at 433 Wh kg^{-1}. A Ragone plot can be helpful at identifying the practical applicability of any given battery. Fig. S7 shows the Ragone plot for all prepared materials and a commercial NCA. Similar trend was found when energy density was plotted against power density as, the prepared NCA-750 had higher energy density and remarkably improved power density at those high C-rates as compared to that of C-NCA. We believe that the overall improvements in the electrochemical performances of our prepared materials, relative to C-NCA, originated from their lower degrees of Ni^{2+} occupancy in Li^+ sites, resulting from lower degrees of cation mixing and further mitigation of Li residue formation on the surface of the cathode material, as suggested by XRD Rietveld refinement analysis.

CV can be useful for identifying phase transitions in electrode materials during charge/discharge processes. Fig. 8a–d displays the first two cycles of the CV curves of the as-prepared NCA samples and C-NCA between 2.5–4.4 V at a very slow scan rate of 0.01 mV s^{-1} in freshly prepared cells. The three anodic and cathodic peaks in the CV cycles correspond to oxidation and reduction between Ni^{2+}/Ni^{4+} and Co^{3+}/Co^{4+}. These peaks represent the three phase transitions occurring during the insertion and removal of Li^+ ions: hexagonal phase to monoclinic phase (H1–M); monoclinic phase to hexagonal phase (M–H2); and hexagonal phase to hexagonal phase (H2–H3) [36].

The polarization potential (ΔV) between the first anodic peak and the cathodic peak of NCA-750 was considerably smaller (219.7 mV) than those of NCA-775 (257.2 mV) and NCA-800 (232.5 mV) and significantly smaller than that of the C-NCA cathode (288.4 mV), indicating higher reversibility of Li^+ ions during the charge/discharge process. The first oxidation peaks in the first cycle shifted to lower potential in the second cycle, due to the formation of the SEI layer, leading to a loss in reversible capacity for the first cycle and decreasing the activation energy barrier for Li^+ ion migration.

We employed EIS to study the effect of the calcination temperature on the electrochemical activity of the cathodes, all of which were tested after three cycling formation (Fig. 9a).

The resulting Nyquist plots featured two regions: a semicircle in the high-frequency range and the straight line in the low-frequency range. Such EIS curves can be fitted to an equivalent circuit model (inset to Fig. 9a), where R_b is the solution bulk resistance, R_{ct} is the charge transfer resistance, CPE is contact phase element, and W_o is the Warburg impedance. The value of R_{ct} is crucial because it represents the resistance to charge transfer within a cathode material. After simulation and fitting, the values of R_{ct} for NCA-750, NCA-775, NCA-800, and C-NCA were 220.3, 252.5, 318.9, and 389.1 Ω, respectively. The resistance at the electrode–electrolyte interface was much lower for the sample that had been calcined at 750 °C, indicating its rapid electron transport during Li^+ insertion/extraction.

We used the following equation to calculate the Li^+ diffusion coefficients, which are listed in Table 4:

$$D_{Li^+} = \frac{R^2T^2}{2A^2n^4f^4c^2\sigma^2} \tag{3}$$

where R is the gas constant, T is the absolute temperature, A is the active area of the cathode, n is the number of electrons transferred during a redox process, F is the Faraday constant, C is the concentration coefficient of Li^+ ions in the electrode, and σ is the Warburg coefficient obtained from the equation

$$Z' = R_s + R_{ct} + \sigma\omega^{-1/2} \tag{4}$$

Fig. 9b reveals the linear relationship between the impedance Z' and the inverse square root of the angular frequency in the low-frequency region. From the slopes (σ) in these plots and eqns (3) and (4), we calculated the values of the coefficients D_{Li}^+ for all of the NCA samples (Table 3). In general, a high value of D_{Li}^+ represents a finely ordered layer morphology in a cathode [35]. The value of D_{Li}^+ for our NCA-750 sample (ca. 1.12×10^{-12} cm^2 s^{-1}) was significantly higher than those of NCA-775 (ca. 9.27×10^{-13} cm^2 s^{-1}) and NCA-800 (ca. 6.88×10^{-13} cm^2 s^{-1}). We suspect that the low calcination

Table 3
Characteristics of previously reported NCA electrodes, compared with those of our best electrode precursor prepared using the CSTR method.

Method (Liter)	Cathode material	Avg precursor size (μm)	Avg oxide particle size (μm)	Capacities (approx.) (mAh g^{-1})		Capacity Retention		Ref
				mAh g^{-1}/C-rate	mAh g^{-1}/C-rate	(%)	Cycles	
CSTR (7)	$LiNi_{0\cdot85}Co_{0\cdot10}Al_{0\cdot05}O_2$	6	5	199/0.1	130/10	79	200	[26]
CSTR (50)	$LiNi_{0\cdot815}Co_{0\cdot15}Al_{0\cdot035}O_2$	12	10	186/0.2	140/5	86	100	[37]
CSTR (2)	$LiNi_{0\cdot80}Co_{0\cdot15}Al_{0\cdot05}O_2$	–	7–8	185/0.1	–	60	200	[30]
CSTR (4)	$LiNi_{0\cdot80}Co_{0\cdot15}Al_{0\cdot05}O_2$	–	–	170/0.2	91/5	91	50	[47]
CSTR (–)	$LiNi_{0\cdot815}Co_{0\cdot15}Al_{0\cdot035}O_2$	10–12	9–10	197/0.1	60/10	75	100	[48]
CTFR (1)	$LiNi_{0\cdot80}Co_{0\cdot15}Al_{0\cdot05}O_2$	6–8	6	190/1	138/10	87	100	This work

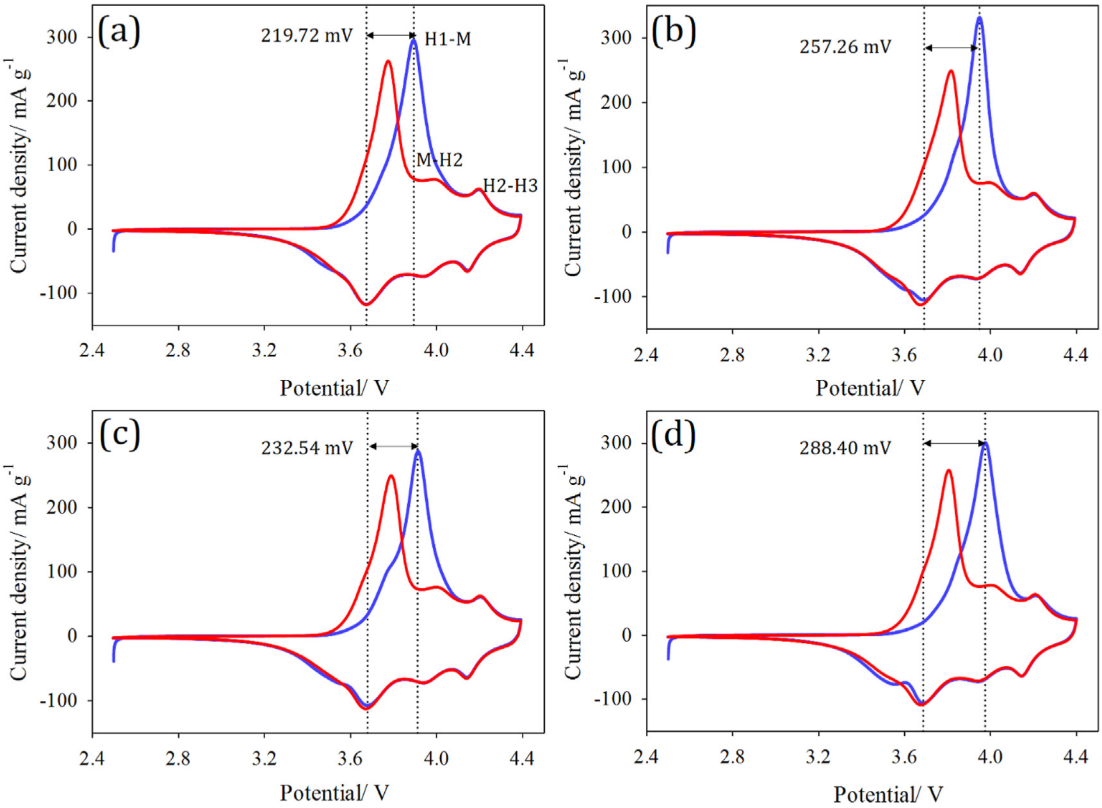

Fig. 8. Cyclic voltammograms (2.5–4.4 V; scan rate: 0.01 mV s^{-1}) of (a–c) the prepared NCA samples at (a) 750, (b) 775, and (c) 800 °C and (d) the commercial NCA sample.

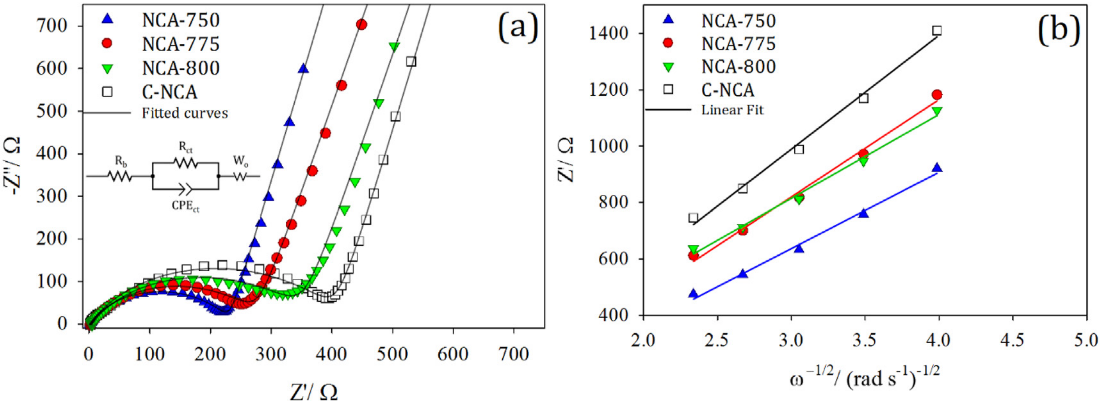

Fig. 9. EIS results of (a) Nyquist plots of all of the samples and (b) linear relationships (slope: σ) between the inverse square root of the angular frequency and the Warburg impedance.

Table 4
Values of R_b and R_{ct} determined from Nyquist plots of all the tested materials and calculated Li$^+$ diffusion coefficients (D_{Li+}).

Sample	R_b (Ω)	R_{ct} (Ω)	σ (Ω s$^{-0.5}$)	D_{Li}^{+}(cm^2 s^{-1})
NCA-750	2.02	220.30	270.35	1.12 × 10^{-12}
NCA-775	2.28	252.50	297.27	9.27 × 10^{-13}
NCA-800	5.44	318.98	345.05	6.88 × 10^{-13}
C-NCA	2.05	389.08	403.31	5.04 × 10^{-13}

temperature of 750 °C caused the particles to grow to an optimal size that facilitated effective migration of Li$^+$ ions into the crystals. Furthermore, the values confirm that our NCA-750 sample had superior structural integrity, due to the compact packing of its primary particles. Thus, the increase in Li$^+$ ion diffusivity could, in turn, enhance the electrochemical performance, due to good crystallinity and a lower degree of cation mixing in the Li slab.

4. Conclusions

We have used CTFR to develop a highly efficient continuous co-precipitation method for the synthesis of Ni-rich NCA hydroxides. The Couette–Taylor flow pattern in the reactor caused the particles to agglomerate and grow uniformly, even after short mean residence times. The rotation speed of the inner cylinder was a crucial parameter affecting the formation of well-shaped spherical NCA hydroxide particles. Furthermore, the calcination temperature played an important role affecting the electrochemical performance of the prepared cathode materials. The sample prepared at 600 rpm, pH 11, and 60 °C, then calcined at 750 °C, delivered a high initial discharge capacity of 190.6 mAh g^{-1}, an extended cycle life, and greatly improved rate capability of 138 mAh g^{-1} at 10C (101 mAh g^{-1} for a typical commercial NCA cathode). This improved performance appeared to be due mainly to the cathode material having an intact shape and structural integrity. EIS and CV revealed that our prepared samples exhibited superior Li^+ ion diffusivity and lower degrees of polarization relative to the commercial sample, presumably because of a uniform distribution of Ni, Co, and Al atoms induced by the unique Taylor-vortex fluid profile in the reactor. Thus, this method is an efficient one for the synthesis of Ni-rich cathode materials of high uniformity and displaying excellent electrochemical activity for potential use in LIBs.

Credit Author Statement

All authors have equally contributed to this manuscript.

Declaration of competing interest

The authors declare that they have no known competing financial interests or personal relationships that could have appeared to influence the work reported in this paper.

Acknowledgement

We thank the Ministry of Science and Technology of Taiwan (project no. MOST 109−3116-F-131−001-CC1) for financial support.

Appendix A. Supplementary data

Supplementary data to this article can be found online at https://doi.org/10.1016/j.jallcom.2020.157594.

References

[1] N. Nitta, F. Wu, J.T. Lee, G. Yushin, Li-ion battery materials: present and future, Mater. Today 18 (2015) 252−264, https://doi.org/10.1016/j.mattod.2014.10.040.

[2] V. Etacheri, R. Marom, R. Elazari, G. Salitra, D. Aurbach, Challenges in the development of advanced Li-ion batteries: a review, Energy Environ. Sci. 4 (2011) 3243−3262, https://doi.org/10.1039/c1ee01598b.

[3] J.B. Goodenough, K.S. Park, The Li-ion rechargeable battery: a perspective, J. Am. Chem. Soc. 135 (2013) 1167−1176, https://doi.org/10.1021/ja3091438.

[4] J.B. Goodenough, Y. Kim, Challenges for rechargeable Li batteries, Chem. Mater. 22 (2010) 587−603, https://doi.org/10.1021/cm901452z.

[5] J.M. Tarascon, M. Armand, Issues and challenges facing rechargeable lithium batteries, Nature 414 (2001) 359-367, https://doi.org/10.1038/35104644.

[6] M.S. Whittingham, History, evolution, and future status of energy storage, Proc. IEEE 100 (2012) 1518−1534, https://doi.org/10.1109/JPROC.2012.2190170.

[7] Y.K. Sun, Z. Chen, H.J. Noh, D.J. Lee, H.G. Jung, Y. Ren, S. Wang, C.S. Yoon, S.T. Myung, K. Amine, Nanostructured high-energy cathode materials for advanced lithium batteries, Nat. Mater. 11 (2012) 942−947, https://doi.org/10.1038/nmat3435.

[8] Y.K. Sun, S.T. Myung, B.C. Park, J. Prakash, I. Belharouak, K. Amine, High-energy cathode material for long-life and safe lithium batteries, Nat. Mater. 8 (2009) 320−324, https://doi.org/10.1038/nmat2418.

[9] H. Liang, Z. Wang, H. Guo, J. Wang, J. Leng, Improvement in the electrochemical performance of $LiNi_{0.8}Co_{0.1}Mn_{0.1}O_2$ cathode material by Li_2ZrO_3 coating, Appl. Surf. Sci. 423 (2017) 1045−1053, https://doi.org/10.1016/j.apsusc.2017.06.283.

[10] Y. Li, H. Yu, Y. Hu, H. Jiang, C. Li, Surface-engineering of layered $LiNi_{0.815}Co_{0.15}Al_{0.035}O_2$ cathode material for high-energy and stable Li-ion batteries, J. Energy Chem. 27 (2018) 559−564, https://doi.org/10.1016/j.jechem.2017.11.004.

[11] Y.K. Sun, S.T. Myung, M.H. Kim, J. Prakash, K. Amine, Synthesis and characterization of $Li[(Ni_{0.8}Co_{0.1}Mn_{0.1})_{0.8}(Ni_{0.5}Mn_{0.5})_{0.2}]O_2$ with the microscale core-shell structure as the positive electrode material for lithium ba, J. Am. Chem. Soc. 127 (2005) 13411−13418, https://doi.org/10.1021/ja053675g.

[12] J.E. Kim, W.S. Kim, Synthesis of Core-Shell Particles of Nickel-Manganese-Cobalt Hydroxides in a Continuous Couette-Taylor Crystallizer, 2017, https://doi.org/10.1021/acs.cgd.7b00225.

[13] Y. Xia, J. Zheng, C. Wang, M. Gu, Designing principle for Ni-rich cathode materials with high energy density for practical applications, Nanomater. Energy 49 (2018) 434−452, https://doi.org/10.1016/j.nanoen.2018.04.062.

[14] X. Li, D. Wang, J. Ru, W. Wang, Z. Wang, H. Guo, Improvement of high voltage electrochemical performance of $LiNi_{0.5}Co_{0.2}Mn_{0.3}O_2$ cathode materials via Li_2ZrO_3 coating, Ceram. Int. 41 (2015) 6663−6667, https://doi.org/10.1016/j.ceramint.2015.01.100.

[15] C.F. Zhang, P. Yang, X. Dai, X. Xiong, J. Zhan, Y.L. Zhang, Synthesis of $LiNi_{1/3}Co_{1/3}Mn_{1/3}O_2$ Cathode Material via Oxalate Precursor, Trans. Nonferrous Met. Soc. China (English Ed. vol. 19 (2009) 635−641, https://doi.org/10.1016/S1003-6326(08)60325-8.

[16] S.H. Ju, H.C. Jang, Y.C. Kang, Al-doped Ni-rich cathode powders prepared from the precursor powders with fine size and spherical shape, Electrochim. Acta 52 (2007) 7286−7292, https://doi.org/10.1016/j.electacta.2007.05.064.

[17] I. Lee, J. Bae, J. Kim, Y.M. Kim, D.H. Ha, H. Son, S. Yoon, Tuning of aluminum concentration distribution in high nickel cathode particles for lithium ion batteries, J. Alloys Compd. (2019) 152677, https://doi.org/10.1016/j.jallcom.2019.152677.

[18] D.K. Thai, Q.P. Mayra, W.S. Kim, Agglomeration of Ni-rich hydroxide crystals in Taylor vortex flow, Powder Technol 274 (2015) 5−13, https://doi.org/10.1016/j.powtec.2015.01.008.

[19] W.M. Jung, S. Hoon Kang, K.S. Kim, W.S. Kim, C. Kyun Choi, Precipitation of calcium carbonate particles by gasliquid reaction: morphology and size distribution of particles in Couette-Taylor and stirred tank reactors, J. Cryst. Growth 312 (2010) 3331−3339, https://doi.org/10.1016/j.jcrysgro.2010.08.026.

[20] M.F. Aljishi, A.C. Ruo, J.H. Park, B. Nasser, W.S. Kim, Y.L. Joo, Effect of flow structure at the onset of instability on barium sulfate precipitation in Taylor-Couette crystallizers, J. Cryst. Growth 373 (2013) 20−31, https://doi.org/10.1016/j.jcrysgro.2012.11.048.

[21] W.K. Park, H. Kim, T. Kim, Y. Kim, S. Yoo, S. Kim, D.H. Yoon, W.S. Yang, Facile synthesis of graphene oxide in a Couette-Taylor flow reactor, Carbon N. Y. 83 (2015) 217−223, https://doi.org/10.1016/j.carbon.2014.11.024.

[22] X. Wei, H. Takahashi, S. Sato, M. Nomura, Continuous emulsion polymerization of styrene in a single Couette-Taylor vortex flow reactor, J. Appl. Polym. Sci. 80 (2001) 1931−1942, https://doi.org/10.1002/app.1291.

[23] W. Xue, K. Yoshikawa, A. Oshima, S. Sato, M. Nomura, Continuous emulsion polymerization of vinyl acetate. II. Operation in a single Couette-Taylor vortex flow reactor using sodium lauryl sulfate as emulsifier, J. Appl. Polym. Sci. 86 (2002) 2755−2762, https://doi.org/10.1002/app.11256.

[24] S.A. Park, S. Lee, W.S. Kim, Polymorphic crystallization of sulfamerazine in Taylor vortex flow: polymorphic nucleation and phase transformation, Cryst. Growth Des. 15 (2015) 3617−3627, https://doi.org/10.1021/acs.cgd.5b00002.

[25] A.-T. Nguyen, T. Yu, W.-S. Kim, Couette-Taylor crystallizer: effective control of crystal size distribution and recovery of l-lysine in cooling crystallization, J. Cryst. Growth 469 (2017) 65−77, https://doi.org/10.1016/j.jcrysgro.2016.10.020.

[26] M. Jo, M. Noh, P. Oh, Y. Kim, J. Cho, A new high power $LiNi_{0.81}Co_{0.1}Al_{0.09}O_2$ cathode material for lithium-ion batteries, Adv. Energy Mater. 4 (2014) 1−8, https://doi.org/10.1002/aenm.201301583.

[27] K. Du, C. Hua, C. Tan, Z. Peng, Y. Cao, G. Hu, A high-powered concentration-gradient $Li(Ni_{0.85}Co_{0.12}Mn_{0.03})O_2$ cathode material for lithium ion batteries, J. Power Sources 263 (2014) 203−208, https://doi.org/10.1016/j.jpowsour.2014.04.047.

[28] J. Zheng, P. Yan, L. Estevez, C. Wang, J.G. Zhang, Effect of calcination temperature on the electrochemical properties of nickel-rich $LiNi_{0.76}Mn_{0.14}Co_{0.10}O_2$ cathodes for lithium-ion batteries, Nanomater. Energy 49 (2018) 538−548, https://doi.org/10.1016/j.nanoen.2018.04.077.

[29] F. Wu, N. Liu, L. Chen, Y. Su, G. Tan, L. Bao, Q. Zhang, Y. Lu, J. Wang, S. Chen, J. Tan, Improving the reversibility of the H2-H3 phase transitions for layered Ni-rich oxide cathode towards retarded structural transition and enhanced cycle stability, Nanomater. Energy 59 (2019) 50−57, https://doi.org/10.1016/j.nanoen.2019.02.027.

[30] N. Wu, H. Wu, H. Liu, Y. Zhang, Solvothermal coating $LiNi_{0.8}Co_{0.15}Al_{0.05}O_2$ microspheres with nanoscale Li_2TiO_3 shell for long lifespan Li-ion battery cathode materials, J. Alloys Compd. 665 (2016) 48−56, https://doi.org/10.1016/j.jallcom.2016.01.044.

[31] U.H. Kim, J.H. Kim, J.Y. Hwang, H.H. Ryu, C.S. Yoon, Y.K. Sun, Compositionally and structurally redesigned high-energy Ni-rich layered cathode for next-generation lithium batteries, Mater. Today 23 (2019) 26−36, https://doi.org/10.1016/j.mattod.2018.12.004.

[32] Y. Su, Y. Yang, L. Chen, Y. Lu, L. Bao, G. Chen, Z. Yang, Q. Zhang, J. Wang, R. Chen, S. Chen, F. Wu, Improving the cycling stability of Ni-rich cathode materials by fabricating surface rock salt phase, Electrochim. Acta 292 (2018) 217−226, https://doi.org/10.1016/j.electacta.2018.09.158.

[33] Z. Qiu, Y. Zhang, P. Dong, S. Xia, Y. Yao, A facile method for synthesis of $LiNi_{0.8}Co_{0.15}Al_{0.05}O_2$ cathode material, Solid State Ionics 307 (2017) 73−78, https://doi.org/10.1016/j.ssi.2017.04.011.

[34] P. Hou, H. Zhang, X. Deng, X. Xu, L. Zhang, Stabilizing the electrode/electrolyte interface of $LiNi_{0.8}Co_{0.15}Al_{0.05}O_2$ through tailoring aluminum distribution in microspheres as long-Life, high-rate, and safe cathode for lithium-ion batteries, ACS Appl. Mater. Interfaces 9 (2017) 29643−29653, https://doi.org/10.1021/acsami.7b05986.

[35] P. Xiao, T. Lv, X. Chen, C. Chang, $LiNi_{0.8}Co_{0.15}Al_{0.05}O_2$: enhanced electrochemical performance from reduced cationic disordering in Li slab, Sci. Rep. 7 (2017) 1408, https://doi.org/10.1038/s41598-017-01657-9.

[36] J. Yuan, J. Wen, J. Zhang, D. Chen, D. Zhang, Influence of calcination atmosphere on structure and electrochemical behavior of $LiNi_{0.6}Co_{0.2}Mn_{0.2}O_2$ cathode material for lithium-ion batteries, Electrochim. Acta 230 (2017) 116–122, https://doi.org/10.1016/j.electacta.2017.01.102.

[37] X. Yang, X. Huang, H. Shi, P. Dong, D. Wang, J. Duan, Y. Zhang, Growth mechanisms for spherical $Ni_{0.815}Co_{0.15}Al_{0.035}(OH)_2$ precursors, J. Energy Chem. 53 (2020) 379–386, https://doi.org/10.1016/j.jechem.2020.05.049.

[38] J. Ying, C. Wan, C. Jiang, Y. Li, Preparation and characterization of high-density spherical $LiNi_{0.8}Co_{0.2}O_2$ cathode material for lithium secondary batteries, J. Power Sources 99 (2001) 78–84, https://doi.org/10.1016/S0378-7753(01)00477-3.

[39] J. Li, W. Zhao, F. Huang, A. Manivannan, N. Wu, Single-crystalline $Ni(OH)_2$ and NiO nanoplatelet arrays as supercapacitor electrodes, Nanoscale 3 (2011) 5103–5109, https://doi.org/10.1039/c1nr10802f.

[40] C.J. Han, J.H. Yoon, W. Il Cho, H. Jang, Electrochemical properties of $LiNi_{0.8}Co_{0.2-x}Al_{x}O_2$ prepared by a sol-gel method, J. Power Sources 136 (2004) 132–138, https://doi.org/10.1016/j.jpowsour.2004.05.006.

[41] Y.S. Meng, G. Ceder, C.P. Grey, W.S. Yoon, Y. Shao-Horn, Understanding the crystal structure of layered $LiNi_{0.5}Mn_{0.5}O_2$ by electron diffraction and powder diffraction simulation, Electrochem. Solid State Lett. 7 (2004) 155–158, https://doi.org/10.1149/1.1718211.

[42] C. Song, W. Wang, H. Peng, Y. Wang, C. Zhao, H. Zhang, Q. Tang, J. Lv, X. Du, Y. Dou, Improving the electrochemical performance of $LiNi_{0.80}Co_{0.15}Al_{0.05}O_2$ in lithium ion batteries by $LiAlO_2$ surface modification, Appl. Sci. 8 (2018) 378, https://doi.org/10.3390/app8030378.

[43] Y. Yamamoto, M. Ohtsuka, Y. Azuma, T. Takahashi, S. Muto, Cation mixing in $LiNi_{0.8}Co_{0.15}Al_{0.05}O_2$ positive electrode material studied using high angular resolution electron channeling X-ray spectroscopy, J. Power Sources 401 (2018) 263–270, https://doi.org/10.1016/j.jpowsour.2018.08.100.

[44] F. Wu, J. Tian, Y. Su, J. Wang, C. Zhang, L. Bao, T. He, J. Li, S. Chen, Effect of Ni^{2+} content on lithium/nickel disorder for Ni-rich cathode materials, ACS Appl. Mater. Interfaces 7 (2015) 7702–7708, https://doi.org/10.1021/acsami.5b00645.

[45] Y. Liu, L. Huang, Z. Ding, J. Wang, J. Wu, H. Zhang, M. Lavorgna, On the tailoring the 1D rod-like hierarchical nano/micro $LiNi_{0.8}Co_{0.15}Al_{0.05}O_2$ structure with exposed (101) plane by template method, J. Alloys Compd. 791 (2019) 356–363, https://doi.org/10.1016/j.jallcom.2019.03.315.

[46] C. Yang, R. Shao, Y. Mi, L. Shen, B. Zhao, Q. Wang, K. Wu, W. Lui, P. Gao, H. Zhou, Stable interstitial layer to alleviate fatigue fracture of high nickel cathode for lithium-ion batteries, J. Power Sources 376 (2018) 200–206, https://doi.org/10.1016/j.jpowsour.2017.11.085.

[47] B. Park, H. Kim, H.J. Bang, J. Prakash, Y. Sun, Improvement of electrochemical performance of $Li[Ni_{0.8}Co_{0.15}Al_{0.05}]O_2$ cathode materials by AlF_3 coating at various temperatures, Ind. Eng. Chem. Res. 47 (2008) 3876–3882, https://doi.org/10.1021/ie0715308.

[48] C.L. Xu, W. Xiang, Z.G. Wu, Y.C. Li, Y. Di Xu, W.B. Hua, X.D. Guo, X.B. Zhang, B.H. Zhong, A comparative study of crystalline and amorphous $Li_{0.5}La_{0.5}TiO_3$ as surface coating layers to enhance the electrochemical performance of $LiNi_{0.815}Co_{0.15}Al_{0.035}O_2$ cathode, J. Alloys Compd. 740 (2018) 428–435, https://doi.org/10.1016/j.jallcom.2017.12.193.